

finite nonpercolating clusters may also be related to shear transformation zones, which are collective rearrangements of atoms during the deformation of metallic glasses (36). This concept is supported by the observation that typical zone sizes (~10 to 20 atoms) (37–39) are close to cluster sizes (~8 atoms). The continuum percolation model illustrates how structure and rigidity may organize in the absence of ordering; atoms percolate in the liquid, and the percolating cluster “freezes” (or jams) into a glass.

## REFERENCES AND NOTES

- C. A. Angell, *Science* **267**, 1924–1935 (1995).
- P. G. Debenedetti, F. H. Stillinger, *Nature* **410**, 259–267 (2001).
- W. Klement, R. H. Willens, P. Duwez, *Nature* **187**, 869–870 (1960).
- M. F. Ashby, A. L. Greer, *Scr. Mater.* **54**, 321–326 (2006).
- D. B. Miracle, *Nat. Mater.* **3**, 697–702 (2004).
- H. W. Sheng, W. K. Luo, F. M. Alamgir, J. M. Bai, E. Ma, *Nature* **439**, 419–425 (2006).
- A. Hirata et al., *Nat. Mater.* **10**, 28–33 (2011).
- J. Sietsma, B. J. Thijssen, *J. Non-Cryst. Solids* **135**, 146–154 (1991).
- A. S. Keys, A. R. Abate, S. C. Glotzer, D. J. Durian, *Nat. Phys.* **3**, 260–264 (2007).
- D. Ma, A. D. Stoica, X. L. Wang, *Nat. Mater.* **8**, 30–34 (2009).
- Q. Zeng et al., *Phys. Rev. Lett.* **112**, 185502 (2014).
- B. B. Mandelbrot, *The Fractal Geometry of Nature (Updated and Augmented Edition)* (W. H. Freeman, New York, 1983).
- T. Tallinen, J. A. Åström, J. Timonen, *Nat. Mater.* **8**, 25–29 (2009).
- X. Ma, M. R. Zachariah, C. D. Zangmeister, *Nano Lett.* **12**, 486–489 (2012).
- D. B. Miracle, *Acta Mater.* **61**, 3157–3171 (2013).
- Y. Q. Cheng, E. Ma, *Prog. Mater. Sci.* **56**, 379–473 (2011).
- G. Duan et al., *Phys. Rev. B* **71**, 224208 (2005).
- Y. Q. Cheng, E. Ma, H. W. Sheng, *Phys. Rev. Lett.* **102**, 245501 (2009).
- M. I. Mendelev et al., *Philos. Mag.* **89**, 967–987 (2009).
- G. P. Purja Pun, Y. Mishin, *Philos. Mag.* **89**, 3245–3267 (2009).
- V. K. S. Shante, S. Kirkpatrick, *Adv. Phys.* **20**, 325–357 (1971).
- M. Sahimi, *Applications of Percolation Theory* (Taylor & Francis, Bristol, PA, 1994).
- A. Bunde, S. Havlin, *Fractals and Disordered Systems* (Springer-Verlag, New York, 1991).
- H. Scher, R. Zallen, *J. Chem. Phys.* **53**, 3759 (1970).
- J. Wang, Z. Zhou, W. Zhang, T. M. Garoni, Y. Deng, *Phys. Rev. E Stat. Nonlin. Soft Matter Phys.* **87**, 052107 (2013).
- M. J. Powell, *Phys. Rev. B* **20**, 4194–4198 (1979).
- C. D. Lorenz, R. M. Ziff, *J. Chem. Phys.* **114**, 3659 (2001).
- A. S. Clarke, J. D. Wiley, *Phys. Rev. B Condens. Matter* **35**, 7350–7356 (1987).
- Materials and methods are available as supplementary materials on Science Online.
- A. J. Liu, S. R. Nagel, *Nature* **396**, 21–22 (1998).
- V. Trappe, V. Prasad, L. Cipelletti, P. N. Segre, D. A. Weitz, *Nature* **411**, 772–775 (2001).
- R. Orbach, *Science* **231**, 814–819 (1986).
- E. R. Weeks, J. C. Crocker, A. C. Levitt, A. Schofield, D. A. Weitz, *Science* **287**, 627–631 (2000).
- Y. Li, Q. Guo, J. A. Kalb, C. V. Thompson, *Science* **322**, 1816–1819 (2008).
- B. Yang, C. T. Liu, T. G. Nieh, *Appl. Phys. Lett.* **88**, 221911 (2006).
- M. L. Falk, J. S. Langer, *Phys. Rev. E Stat. Phys. Plasmas Fluids Relat. Interdiscip. Topics* **57**, 7192–7205 (1998).
- M. L. Falk, *Phys. Rev. B* **60**, 7062–7070 (1999).
- A. C. Lund, C. A. Schuh, *Acta Mater.* **51**, 5399–5411 (2003).
- F. Delogu, *Phys. Rev. Lett.* **100**, 255901 (2008).

## ACKNOWLEDGMENTS

Diffraction data and simulated RDFs are available as supplementary materials. The authors thank D. C. Hofmann for providing the  $\text{Cu}_{46}\text{Zr}_{46}\text{Al}_5\text{Be}_3$  wires and Y. Lin for her aid in sample loading. The authors acknowledge the financial support of the U.S. Department of Energy Office of Basic Energy Sciences (DOE-BES) and NASA's Space Technology Research Grants Program (Early Career Faculty grants to J.R.G.). W.L.M. and C.Y.S. acknowledge support from NSF grant EAR-1055454. Q.Z. acknowledges support from DOE-BES (grant DE-FG02-99ER45775) and the National

Natural Science Foundation of China (grant U1530402). Portions of this work were performed at the High Pressure Collaborative Access Team (HPCAT) of the Advanced Photon Source (APS), Argonne National Laboratory. HPCAT operations are supported by DOE's National Nuclear Security Administration (NNSA) under award no. DE-NA0001974 and by DOE-BES under award no. DE-FG02-99ER45775, with partial instrumentation funding by NSF grant MRI-1126249. APS is supported by DOE-BES under contract no. DE-AC02-06CH11357. Portions of this research were carried out at the Stanford Synchrotron Radiation Lightsource, a directorate of SLAC National Accelerator Laboratory and an Office of Science User Facility operated for DOE by Stanford University. Some computations were carried out on the Shared Heterogeneous Cluster computers (Caltech Center for Advanced Computing Research) provided by the NNSA Predictive Science Academic Alliance Program at Caltech (grant DE-FC52-08NA28613) and on the NSF Center for Science and Engineering of Materials computer cluster (grant DMR-0520565). Q.A. and W.A.G. received support from the Defense Advanced Research

Projects Agency–Army Research Office (grant W31P4Q-13-1-0010) and NSF (grant DMR-1436985). This material is based on work supported by an NSF Graduate Research Fellowship (grant DGE-1144469). Any opinions, findings, and conclusions or recommendations expressed in the material are those of the authors and do not necessarily reflect the views of NSF.

## SUPPLEMENTARY MATERIALS

www.sciencemag.org/content/349/6254/1306/suppl/DC1  
Materials and Methods  
Supplementary Text  
Figs. S1 to S3  
References (40–42)  
Databases S1 to S4

14 March 2015; accepted 31 July 2015  
10.1126/science.aab1233

## APPLIED OPTICS

# An ultrathin invisibility skin cloak for visible light

Xingjie Ni,<sup>1\*</sup> Zi Jing Wong,<sup>1\*</sup> Michael Mrejen,<sup>1</sup> Yuan Wang,<sup>1,2</sup> Xiang Zhang<sup>1,2,3,†</sup>

Metamaterial-based optical cloaks have thus far used volumetric distribution of the material properties to gradually bend light and thereby obscure the cloaked region. Hence, they are bulky and hard to scale up and, more critically, typical carpet cloaks introduce unnecessary phase shifts in the reflected light, making the cloaks detectable. Here, we demonstrate experimentally an ultrathin invisibility skin cloak wrapped over an object. This skin cloak conceals a three-dimensional arbitrarily shaped object by complete restoration of the phase of the reflected light at 730-nanometer wavelength. The skin cloak comprises a metasurface with distributed phase shifts rerouting light and rendering the object invisible. In contrast to bulky cloaks with volumetric index variation, our device is only 80 nanometer (about one-ninth of the wavelength) thick and potentially scalable for hiding macroscopic objects.

A cloak is a device that can render objects invisible to incoming waves. Transformation optics and metamaterials provide powerful tools to build cloaking devices. Different schemes relying either on coordinate transformation (1–3) or scattering cancellation (4–6) have been studied. Although the concept was first proposed for electromagnetic waves, soon it was extended to acoustic waves (7), heat flows (8–10), elastic or seismic waves (11–13), and even the matter waves (14, 15). A quasi-conformal mapping technique (16) was used to design a so-called carpet cloak that conceals an object by restoring the wavefront as if it were reflected from a flat surface. This technique relaxes the requirements of hard-to-achieve material properties and anisotropy as in the case of the original cloak, thereby making it easier to design and fabricate. Such invisibility carpet cloaks were demonstrated experimentally from microwave (17) to optical frequencies (18–23). Never-

theless, there are still substantial limitations in current optical cloak designs that apply the quasi-conformal mapping technique. Realization requires refractive index modulation over a large volume to avoid extremely high or low index, leading to a bulky cloak. In addition, sophisticated three-dimensional (3D) fabrication with very high spatial resolution is necessary. Therefore, it is challenging to scale up this design to macroscopic sizes. In addition, the varying index has to be less than that of the environment in certain regions (Fig. 1C), making it difficult to create a cloak that works in air. As a result, the cloak is usually embedded in a dielectric prism of higher index which, however, introduces an additional phase in the reflected light and makes the optical cloak itself visible by phase-sensitive detection.

Recent development of metasurfaces pointed out a way to manipulate the phase of a propagating wave directly. The metasurface is an optically thin layer consisting of subwavelength-sized elements that locally tailor the electromagnetic response at the nanoscale accompanied by dramatic light confinement (24–30). Metasurfaces have enabled a variety of unique phenomena and applications that cannot be achieved conventionally (31, 32)—for example, negative-angle refraction in a broad

<sup>1</sup>NSF Nanoscale Science and Engineering Center (NSEC), University of California, Berkeley, CA 94720, USA. <sup>2</sup>Materials Sciences Division, Lawrence Berkeley National Laboratory, Berkeley, CA 94720, USA. <sup>3</sup>Department of Physics, King Abdulaziz University, Jeddah 21589, Saudi Arabia.

\*These authors contributed equally to this work. †Corresponding author. E-mail: xiang@berkeley.edu

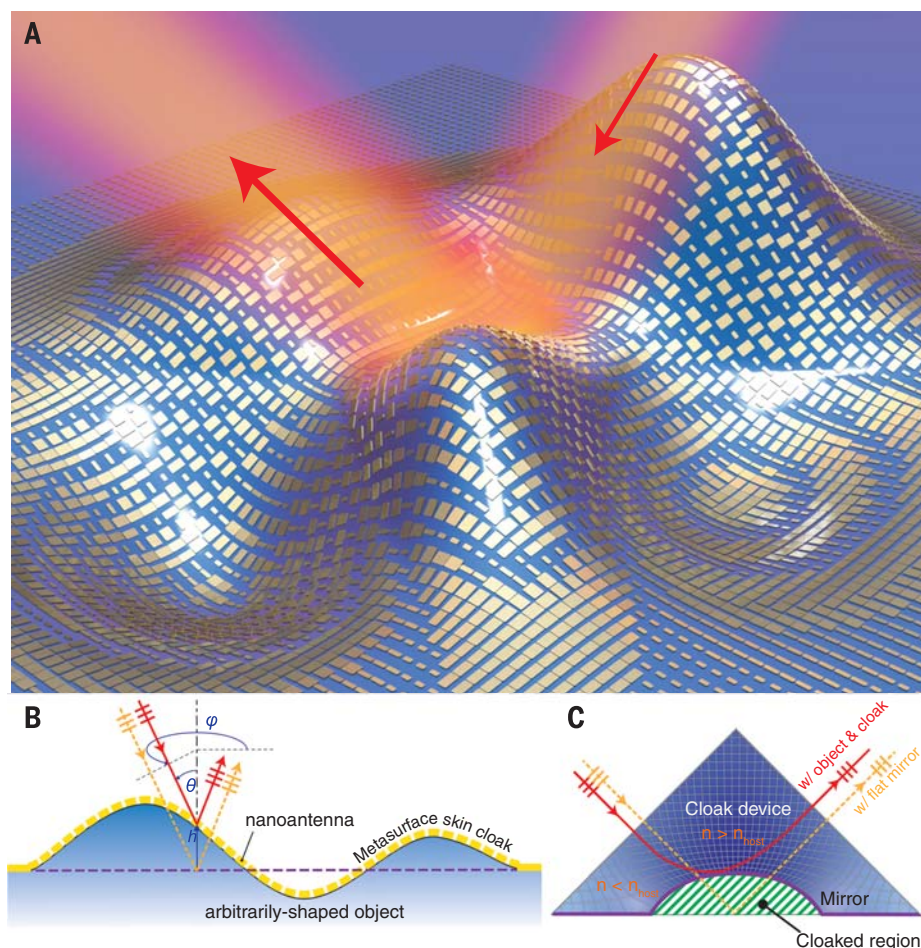


**Fig. 1. Schematic view and working principle of a metasurface skin cloak.** (A) A 3D illustration of a metasurface skin cloak. The skin cloak is an ultrathin layer of nanoantennas (gold blocks) covering the arbitrarily shaped object. (B) Schematic view of a cross section of the metasurface skin cloak. (C) Schematic illustration of a conventional carpet cloak with spatially varying refractive index ( $n$ ), designed with an optical quasi-conformal mapping technique. The blue shading qualitatively indicates the local refractive index (the darker color indicates higher index) and the grid lines indicate the deformed optical space. For both devices, the light is incident from the left and exits to the right as represented by the arrows. The devices recover the wavefront (indicated as triple short lines) of the exiting light, such that the object is hidden and looks like a flat mirror, judging from the scattering pattern of the exiting light. However, a conventional cloak introduces additional phase retardation due to the light propagation inside its host material, which renders it detectable to a phase-sensitive measuring device. In contrast, the metasurface skin cloak fully restores both the wavefront and the phase of the scattered light and thus the object is perfectly hidden. On the metasurface skin cloak, a phase shift provided by each nanoantenna realigns the wavefront. At an arbitrary point on the object with height  $h$  to the flat reference plane, the nanoantenna should recover the phase of the scattered light. Light (red solid lines) incident at an oblique angle  $(\theta, \phi)$  at that point should scatter as if it were reflected by the reference plane (orange dashed lines). The nanoantenna at that point should provide a phase shift  $\Delta\Phi = -2k_0 h \cos\theta + \pi$ , which compensates the phase difference between the solid and dashed lines. Note that the height is negative when the surface is below the reference plane.

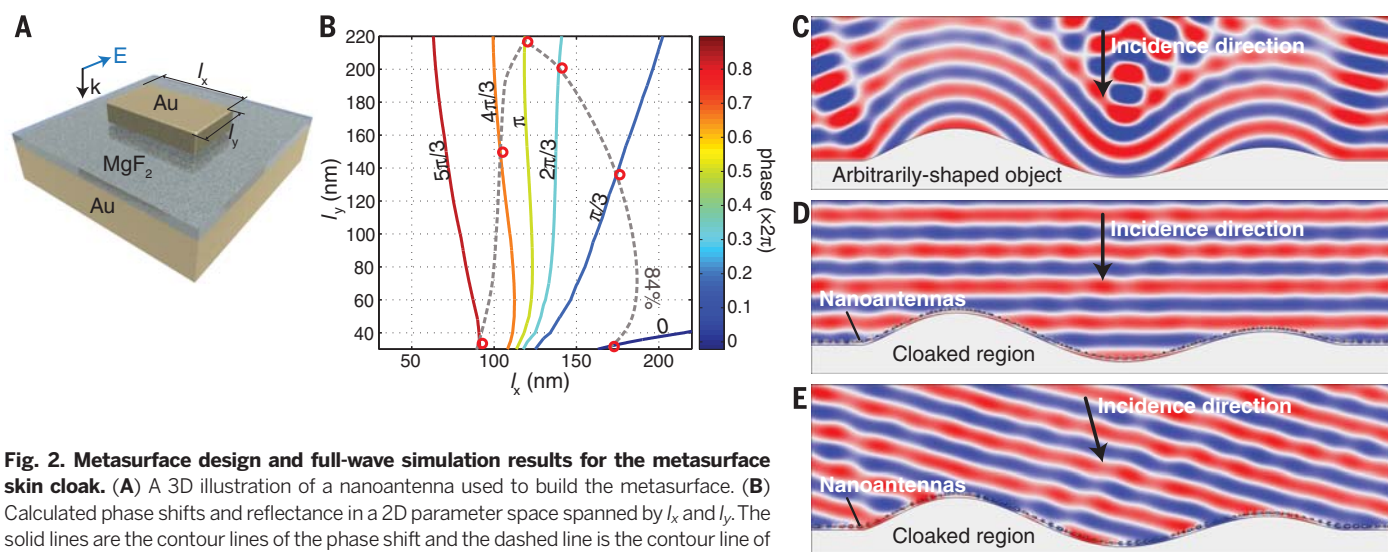


**Fig. 2. Metasurface design and full-wave simulation results for the metasurface skin cloak.** (A) A 3D illustration of a nanoantenna used to build the metasurface. (B) Calculated phase shifts and reflectance in a 2D parameter space spanned by  $l_x$  and  $l_y$ . The solid lines are the contour lines of the phase shift and the dashed line is the contour line of the reflectance at 84%. For simplicity, six different nanoantennas, which span the phase from 0 to  $2\pi$  with an interval of  $\pi/3$ , are chosen as the building blocks to construct the metasurface, as shown by the six red circles intersecting the phase and the 84%-reflectance contour lines. (C) to (E) Full-wave simulated electrical field distribution (shown for a cross section) based on an actual design for (C) a scattering object without a metasurface skin cloak at normal incidence, (D) the same object with a metasurface skin cloak at normal incidence, and (E) the same object with the same metasurface skin cloak as in (D) but at 15° oblique incidence. Only the reflected field is plotted for clarity. The wavelength of the incident light is 730 nm in the simulation. The reflected light is almost completely recovered by the skin cloak as if there were no scattering object for both normal and oblique incidences.



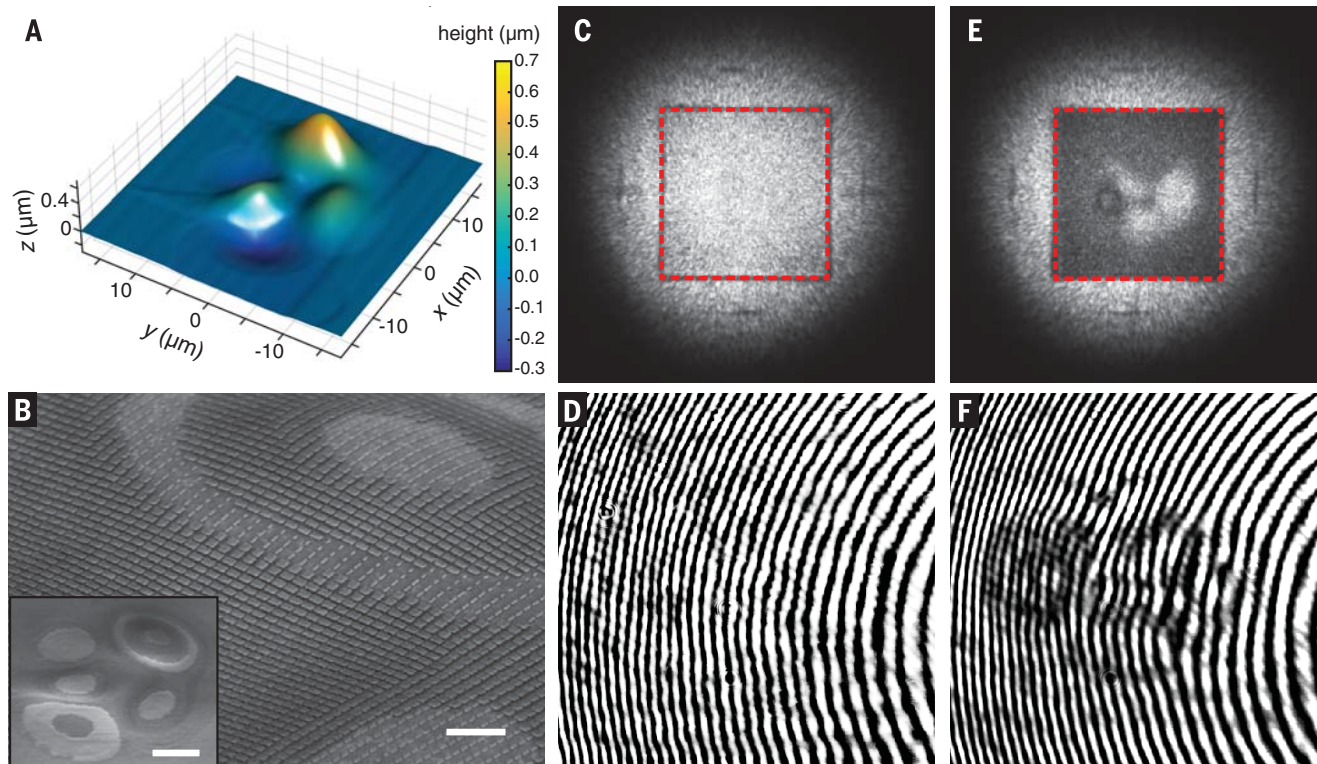


**Fig. 3. A metasurface invisibility skin cloak for a 3D arbitrarily shaped object.** (A) An AFM image of a 3D arbitrarily shaped object that includes multiple bumps and dents. (B) A SEM image of the object onto which a metasurface skin cloak has been fabricated. The scale bar is 1  $\mu\text{m}$ . The inset shows an enlarged image of the entire object, with a scale bar of 5  $\mu\text{m}$ . (C and E) Optical widefield reflection images obtained with a 0.3 numerical aperture objective lens with 730-nm-wavelength laser illumination. The sample region is indicated by the red dashed boxes. (C) The obtained reflection image when

the cloak is on and (E) when the cloak is off, taken at the same position. The noise in the images arises from the laser speckle. (D and F) The respective interference images when the cloak is on and when it is off. When the cloak is off, the interference fringes are distorted on the 3D object, which indicates the height difference on the surface. When the cloak is on, the interference fringes smoothen again, matching with that of the flat surface outside the object region, thus proving that both the wavefront and the phase are well restored without any distortion.

wavelength range (24, 25), unidirectional surface wave coupling (26, 33), planar optical lenses and waveplates (27, 34–37), ultrathin high-resolution holograms (38–40), and enhancement of nonlinear optical responses (41).

Here, we experimentally demonstrate an ultrathin invisibility skin cloak (Fig. 1A) at  $\sim 730$  nm that overcomes the limitations of a bulky cloak. We created a metasurface tightly wrapped over an object to render it free from optical detection. In contrast to the previous bulky design using continuous refractive index distribution over a volumetric space (16), the ultrathin layer of this skin cloak reroutes the light and restores the wavefront scattered from the object by compensating the phase difference using phase-shifting resonant elements on the cloak surface. With the complete wavefront and phase recovery, we are able to conceal, for a specific light polarization, a 3D object of arbitrary shape using this skin cloak. Our device has a thickness of 80 nm ( $\sim \lambda/9$ ) and, being two-dimensional, has much better scalability prospects. Our experiments show that it successfully hides an arbitrarily shaped 3D object of 36  $\mu\text{m}$  by 36  $\mu\text{m}$  at  $\sim 730$ -nm wavelength, both from direct widefield imaging and phase-sensitive detection.

Our metasurface skin cloak consists of sub-wavelength-scale nanoantennas, which provide

distinct phase shifts locally to the reflected electromagnetic waves. On the basis of this phase control capability, we designed the metasurface so that the phase of the scattered light, at each point on the surface of the cloak, would be the same as that of light reflected from a flat mirror. For an oblique-angle  $(\theta, \phi)$  light incident on an arbitrarily shaped 3D object at a height of  $h$  with respect to the reference plane (Fig. 1B), the introduced phase shift should compensate the phase difference between the light scattered by the object and that reflected from the reference plane. It is straightforward to calculate the phase difference, which is  $\Delta\Phi = -2k_0 h \cos\theta + \pi$ , where  $k_0$  is the free space wave number. The additional  $\pi$  term represents the phase jump induced by a reflecting mirror. Therefore, nanoantennas designed with local  $\Delta\Phi$  phase shift should realign the scattered wavefront. Moreover, the phase should be completely restored, rendering the object undetectable even for phase-sensitive instruments.

As a demonstration, we used a simple rectangular nanoantenna design (Fig. 2A). The calculated phase shifts and reflectance in a 2D parameter space spanned by nanoantenna dimensions  $l_x$  and  $l_y$  are mapped out for the selection of designs. Six different antennas with phase shifts covering 0 to  $2\pi$  while preserving the same reflectance were chosen

as the building blocks of the metasurface skin cloak. To make the invisibility cloak fully operable required the reflected intensity to be close to that of a mirror. With adaptation of an ultrathin dielectric spacer layer to create a gap plasmon resonance (42, 43), our antennas were designed to attain an overall reflectivity of 84% at around 730-nm wavelength. The parameters for the nanoantennas used in our experiment are indicated as red circles in Fig. 2B. We built a metasurface using those nanoantennas to compensate the local phase change of the reflection. Full-wave simulation results show that strong scattering and substantial wavefront and phase distortion can occur for an arbitrarily shaped 3D object with a maximum height of about 1  $\mu\text{m}$  and a width of about 10  $\mu\text{m}$  (Fig. 2C). However, by wrapping the object with the metasurface skin cloak, the wavefront and phase are completely restored for both normal (Fig. 2D) and slightly oblique incidences (Fig. 2E). Therefore, the object is perfectly hidden even from phase-sensitive detection.

For experimental realization, we used focused ion beam (FIB) to carve out an arbitrarily shaped 3D object with multiple bumps and dents, as illustrated in Fig. 1A. The height profile was mapped out by an atomic force microscope (AFM), and the metasurface skin cloak was then designed on

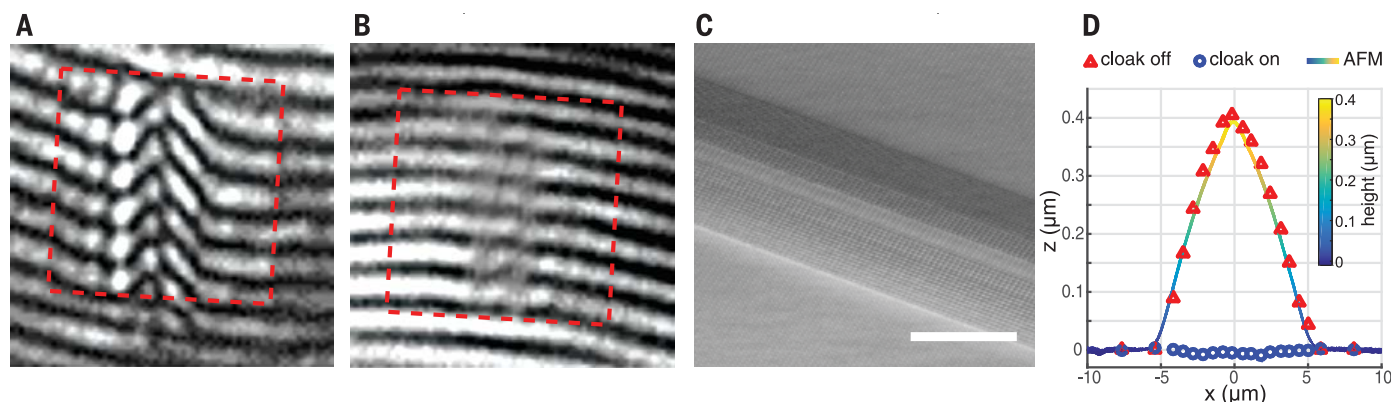


**Fig. 4. Quantitative performance evaluation for a metasurface skin cloak on a 3D bump-shaped object.** The bump-shaped object has a maximum height of  $\sim 400$  nm and a width of  $\sim 10$   $\mu\text{m}$ . (A and B) Interference fringes obtained when the cloak is respectively off and on. The sample regions are indicated by the red dashed boxes. (C) A SEM image of the bump-shaped object with the metasurface skin cloak wrapped over it. The scale bar is 5  $\mu\text{m}$ . (D) The extracted height profile from the interference measurement ( $\Delta$  for cloak off and  $\circ$  for cloak on) together with that from the AFM measurement (solid line) before fabrication of the nanoantennas.

the basis of this measured height profile (Fig. 3A). The mask was fabricated by means of electron beam lithography with precise alignment. More fabrication details can be found in the supplementary materials. Figure 3B shows the scanning electron microscope (SEM) images of the fabricated metasurface masked on the 3D object. The first test was done by obtaining the widefield reflection image of the device. Because we design our nanoantennas to have the correct phase shift only in the  $x$  polarization, we could easily turn the cloak on and off by switching the polarization. With the cloak off, a strong contrast between the cloaked region and the surrounding reflective surface revealed the object (Fig. 3E), but with the correct polarization, the contrast became indistinguishable, rendering the object completely invisible (Fig. 3C). For the phase measurement, a customized Mach-Zehnder interferometer was built (fig. S2) to obtain the reflected phase information from the sample. With the cloak off, there were distortions in the interference fringes indicating nonuniformity in the phase of the reflected light due to the scattering of the object (Fig. 3F). With the cloak on, the distortions disappeared and the fringes were smoothly aligned, indicating that the reflected phase was perfectly uniform over the surface (Fig. 3D). Because we used an objective to image the sample, the interference fringes are rings rather than perfectly straight lines. We also tested an object with an identical profile but without a skin cloak. The interference results (fig. S3B) show fringe distortions similar to those obtained when the cloak is turned off, thereby verifying that the distortion of fringes was purely due to the object scattering and not the metasurface's polarization dependence.

To quantify the performance of a skin cloak, we fabricated and measured a 3D bump-shaped object (Fig. 4). When the cloak was off (Fig. 4A), the interference fringes shifted in the direction perpendicular to the stripes. The extent of phase shift was approximately proportional to the local height of the bump surface. When the cloak was on (Fig. 4B), the interference fringes became smooth and

realigned with those from the flat region. No phase jump was observed even at the edges of the skin cloak, proving that there was no additional phase introduced by the cloak. The relative height information was extracted from the extent of fringe dislocation and compared with the AFM height profile measured before the nanoantennas were fabricated (Fig. 4D). When the skin cloak was off, the height from the interference measurement matched well with the AFM results, revealing the true bump profile. Thus, the bump could be precisely mapped out with the use of this phase-sensitive method. When the cloak was on, the extracted height notably dropped to zero over the entire area.

Our skin cloak fully encompasses the advantages associated with metasurfaces. It is extremely thin, because antenna and dielectric spacer thicknesses are 30 and 50 nm, respectively. With a total thickness of only about  $1/10$  of the operating wavelengths, it is fully scalable to macroscopic sizes. Theoretically, there is no size limitation, yet in practice, the size can be limited by the macroscopic nanofabrication technology. Nevertheless, meter-scale nanofabrication is now possible—for example, by roll-to-roll nano-imprinting. The cloak can also conceal objects with sharp features like abrupt edges and peaks because the invisibility is attained via local phase adjustments. It is worth pointing out that it is not a strict requirement to put the antennas directly on the object. The metasurface can be on a container of any shape, with or without space between the metasurface and the hidden object. As long as the metasurface is designed correctly, both the container and the objects inside the container will become invisible. In our experiment, we chose to fabricate the antennas right on top of the object to demonstrate the extreme capability of ultrathin 3D cloaking of an arbitrary shape. Our design tolerated incident angles at least within  $30^\circ$ . To allow easy switching between cloak on and cloak off configurations for direct comparison, the metasurface was designed to work only in one polarization. However, by

making the nanoantenna shapes symmetric in both  $x$  and  $y$  directions, it would be possible to implement a polarization-independent invisibility skin cloak. Furthermore, if the nanoantennas could be made adaptive, passively or actively, a deformable skin cloak could potentially conceal any object.

**Note added in proof:** While this manuscript was in preparation, two theoretical proposals also suggested the use of a phase gradient metasurface to build an invisibility device (44, 45).

## REFERENCES AND NOTES

1. J. B. Pendry, D. Schurig, D. R. Smith, *Science* **312**, 1780–1782 (2006).
2. D. Schurig et al., *Science* **314**, 977–980 (2006).
3. W. S. Cai, U. K. Chettiar, A. V. Kildishev, V. M. Shalae, *Nat. Photonics* **1**, 224–227 (2007).
4. A. Alù, *Phys. Rev. B* **80**, 245115 (2009).
5. P. Y. Fan et al., *Nat. Photonics* **6**, 380–385 (2012).
6. M. Selvanayagam, G. V. Eleftheriades, *Phys. Rev. X* **3**, 041011 (2013).
7. L. Sanchis et al., *Phys. Rev. Lett.* **110**, 124301 (2013).
8. T. Han et al., *Phys. Rev. Lett.* **112**, 054302 (2014).
9. H. Xu, X. Shi, F. Gao, H. Sun, B. Zhang, *Phys. Rev. Lett.* **112**, 054301 (2014).
10. R. Schittny, M. Kadic, S. Guenneau, M. Wegener, *Phys. Rev. Lett.* **110**, 195901 (2013).
11. G. W. Milton, M. Briane, J. R. Willis, *New J. Phys.* **8**, 248 (2006).
12. M. Farhat, S. Guenneau, S. Enoch, *Phys. Rev. Lett.* **103**, 024301 (2009).
13. M. Brun, S. Guenneau, A. B. Movchan, *Appl. Phys. Lett.* **94**, 061903 (2009).
14. S. Zhang, D. A. Genov, C. Sun, X. Zhang, *Phys. Rev. Lett.* **100**, 123002 (2008).
15. R. Fleury, A. Alù, *Phys. Rev. B* **87**, 045423 (2013).
16. J. Li, J. B. Pendry, *Phys. Rev. Lett.* **101**, 203901 (2008).
17. H. F. Ma, T. J. Cui, *Nat. Commun.* **1**, 21 (2010).
18. J. Valentine, J. Li, T. Zentgraf, G. Bartal, X. Zhang, *Nat. Mater.* **8**, 568–571 (2009).
19. L. H. Gabrielli, J. Cardenas, C. B. Poitras, M. Lipson, *Nat. Photonics* **3**, 461–463 (2009).
20. T. Ergin, N. Stenger, P. Brenner, J. B. Pendry, M. Wegener, *Science* **328**, 337–339 (2010).
21. M. Gharghi et al., *Nano Lett.* **11**, 2825–2828 (2011).
22. B. Zhang, Y. Luo, X. Liu, G. Barbastathis, *Phys. Rev. Lett.* **106**, 033901 (2011).
23. X. Chen et al., *Nat. Commun.* **2**, 176 (2011).
24. N. Yu et al., *Science* **334**, 333–337 (2011).
25. X. Ni, N. K. Emani, A. V. Kildishev, A. Boltasseva, V. M. Shalae, *Science* **335**, 427 (2012).



26. S. Sun *et al.*, *Nat. Mater.* **11**, 426–431 (2012).
27. X. Ni, S. Ishii, A. V. Kildishev, V. M. Shalae, *Light Sci. Appl.* **2**, e72 (2013).
28. L. Huang *et al.*, *Light Sci. Appl.* **2**, e70 (2013).
29. N. Shitrit *et al.*, *Science* **340**, 724–726 (2013).
30. X. Yin, Z. Ye, J. Rho, Y. Wang, X. Zhang, *Science* **339**, 1405–1407 (2013).
31. A. V. Kildishev, A. Boltasseva, V. M. Shalae, *Science* **339**, 1232009 (2013).
32. N. Yu, F. Capasso, *Nat. Mater.* **13**, 139–150 (2014).
33. J. Lin *et al.*, *Science* **340**, 331–334 (2013).
34. D. Lin, P. Fan, E. Hasman, M. L. Brongersma, *Science* **345**, 298–302 (2014).
35. F. Aieta *et al.*, *Nano Lett.* **12**, 4932–4936 (2012).
36. N. Yu *et al.*, *Nano Lett.* **12**, 6328–6333 (2012).
37. A. Pors, M. G. Nielsen, S. I. Bozhevolnyi, *Opt. Lett.* **38**, 513–515 (2013).
38. L. Huang *et al.*, *Nat. Commun.* **4**, 3808 (2013).
39. X. Ni, A. V. Kildishev, V. M. Shalae, *Nat. Commun.* **4**, 2807 (2013).
40. G. Zheng *et al.*, *Nat. Nanotechnol.* **10**, 308–312 (2015).
41. J. Lee *et al.*, *Nature* **511**, 65–69 (2014).
42. A. Pors, O. Albrektsen, I. P. Radko, S. I. Bozhevolnyi, *Sci. Rep.* **3**, 2155 (2013).
43. S. Sun *et al.*, *Nano Lett.* **12**, 6223–6229 (2012).
44. N. Mohammadi Estakhri, A. Alù, *IEEE Antennas Wirel. Propag. Lett.* **13**, 1775–1778 (2015).
45. L. Y. Hsu, T. Lepetit, B. Kante, *Prog. Electromagnetics Res.* **152**, 33–40 (2015); [www.jpier.org/PIER/pier.php?paper=15032005](http://www.jpier.org/PIER/pier.php?paper=15032005).

## ACKNOWLEDGMENTS

The work was supported by the U.S. Department of Energy, Office of Science, Basic Energy Sciences, Materials Sciences and Engineering Division under contract no. DE-AC02-05CH11231.

## SUPPLEMENTARY MATERIALS

[www.sciencemag.org/content/349/6254/1310/suppl/DC1](http://www.sciencemag.org/content/349/6254/1310/suppl/DC1)  
Materials and Methods  
Figs. S1 to S5  
Reference (46)

1 July 2015; accepted 17 August 2015  
10.1126/science.aac9411

## FERROELECTRICS

# Emergence of room-temperature ferroelectricity at reduced dimensions

D. Lee,<sup>1</sup> H. Lu,<sup>2</sup> Y. Gu,<sup>3</sup> S.-Y. Choi,<sup>4</sup> S.-D. Li,<sup>5</sup> S. Ryu,<sup>1</sup> T. R. Paudel,<sup>2</sup> K. Song,<sup>6</sup> E. Mikhchev,<sup>7</sup> S. Lee,<sup>1</sup> S. Stemmer,<sup>7</sup> D. A. Tenne,<sup>8</sup> S. H. Oh,<sup>6</sup> E. Y. Tsymlal,<sup>2</sup> X. Wu,<sup>5</sup> L.-Q. Chen,<sup>3</sup> A. Gruverman,<sup>2\*</sup> C. B. Eom<sup>1\*</sup>

The enhancement of the functional properties of materials at reduced dimensions is crucial for continuous advancements in nanoelectronic applications. Here, we report that the scale reduction leads to the emergence of an important functional property, ferroelectricity, challenging the long-standing notion that ferroelectricity is inevitably suppressed at the scale of a few nanometers. A combination of theoretical calculations, electrical measurements, and structural analyses provides evidence of room-temperature ferroelectricity in strain-free epitaxial nanometer-thick films of otherwise nonferroelectric strontium titanate (SrTiO<sub>3</sub>). We show that electrically induced alignment of naturally existing polar nanoregions is responsible for the appearance of a stable net ferroelectric polarization in these films. This finding can be useful for the development of low-dimensional material systems with enhanced functional properties relevant to emerging nanoelectronic devices.

Low-dimensional ferroelectric structures hold a great potential for scientific and technological endeavors (1). Reducing size while retaining ferroelectric properties enables an increase in the storage capacity of non-volatile ferroelectric memories (2), exploration of diverse nanoelectronic functions (3–7), and discovery of exotic physical phenomena (8, 9). However, maintaining the ferroelectricity in low-dimensional structures, such as ultrathin films, has been hampered by depolarization effects (10–12), which

arise from the uncompensated charges at the interface. The strong scaling effect seems to inevitably suppress ferroelectricity and its functions below a critical dimension (10–13). A recent theoretical work suggested an intriguing concept for reversibly enhancing ferroelectricity in ultrathin ferroelectric capacitors via the tailoring of chemical bonds at the metal/oxide interface (14), but this mechanism has not yet been experimentally confirmed.

Here, we describe a different mechanism, which enables enhancement of ferroelectricity as the thickness of the system is decreased. In our approach, we use naturally existing polar nanoregions (PNRs)—local nanometer-sized polar clusters—in an archetype dielectric material with perovskite structure: strontium titanate (SrTiO<sub>3</sub>). PNRs are generally believed to arise from local nanoscale inhomogeneities (such as chemical or structural disorder) (15, 16), which exist in every material (17). For example, Sr vacancies are intrinsic point defects in SrTiO<sub>3</sub> because of their small formation energy (18, 19), comparable with that of oxygen vacancies, which are likely to act as a natural source of PNRs (Fig. 1A) (20, 21). It has been previously shown (20) that relatively thick (tens of nanometers) films of SrTiO<sub>3</sub> exhibit relaxor behavior at low temperatures because of the presence of the

PNRs. We demonstrate that electrically induced alignment and stabilization of PNRs in nanometer-thick SrTiO<sub>3</sub> films results in the emergence of net ferroelectric polarization at room temperature.

Calculations predict that when SrTiO<sub>3</sub> is deficient in Sr, antisite Ti defects could instantaneously form and generate local dipole moments by an off-centering displacement (Fig. 1C) (22). Our first-principles density-functional theory (DFT) modeling (23) shows that the energy gain from this Ti off-centering is as large as ~0.5 eV, originating from structural distortion driven by an ionic radii difference between Ti<sup>2+</sup> (0.86 Å) and Sr<sup>2+</sup> (1.44 Å). A local polarization profile around the antisite Ti atom (Fig. 1D) indicates that the off-centered antisite Ti atom induces a large local polarization in its residing unit cell and coherently polarizes the surrounding region. The polarization switchability follows from a calculated energy barrier of ~0.1 eV between the polarization states (Fig. 1E), which is comparable with a double-well potential barrier in conventional ferroelectric materials (24). Thus, although pure bulk SrTiO<sub>3</sub> is centrosymmetric and nonpolar (25), the PNRs of nanometer-characteristic size can naturally form because of the intrinsic Sr deficiency in SrTiO<sub>3</sub>.

We have previously observed Sr deficiency and associated PNRs even in nominally stoichiometric SrTiO<sub>3</sub> bulk single crystals and films (20, 21). These small-sized PNRs, however, do not necessarily generate ferroelectricity. When the film thickness *t* is much larger than the average PNR size  $\xi$  (Fig. 1A), PNRs are isolated in an insulating matrix. The depolarization field *E<sub>d</sub>* in PNRs cannot be effectively screened and thus destabilizes the polarization of PNRs. On the other hand, as *t* is decreased the PNRs can play a vital role in the emergence of ferroelectricity (Fig. 1B). When *t* becomes comparable with or smaller than  $\xi$ , the electrical boundary conditions for PNRs drastically change as their interfaces come in contact with metallic electrodes and/or become exposed to surface adsorbates. The external charges screen the *E<sub>d</sub>* by compensating for the polarization charge and thus can allow a switchable and stable polarization in PNRs. Such dimensional engineering of polarization stability in PNRs would provide an unconventional way to create and enhance ferroelectricity at reduced dimensions, distinct from methods such as strain (26–28) and interface (13, 14) engineering.

<sup>1</sup>Department of Materials Science and Engineering, University of Wisconsin–Madison, Madison, WI 53706, USA.

<sup>2</sup>Department of Physics and Astronomy and Nebraska Center for Materials and Nanoscience, University of Nebraska, Lincoln, NE 68588, USA. <sup>3</sup>Department of Materials Science and Engineering, Pennsylvania State University, University Park, PA 16802 USA. <sup>4</sup>Department of Materials Modeling and Characterization, Korea Institute of Materials Science, Changwon 642-831, Korea. <sup>5</sup>Department of Physics, Temple University, Philadelphia, PA 19122, USA. <sup>6</sup>Department of Materials Science and Engineering, Pohang University of Science and Technology, Pohang 790-784, Korea. <sup>7</sup>Materials Department, University of California–Santa Barbara, Santa Barbara, CA 93106-5050, USA. <sup>8</sup>Department of Physics, Boise State University, Boise, ID 83725-1570, USA.

\*Corresponding author. E-mail: [agruverman2@unl.edu](mailto:agruverman2@unl.edu) (A.G.); [eom@engr.wisc.edu](mailto:eom@engr.wisc.edu) (C.B.E.)

## An ultrathin invisibility skin cloak for visible light

Xingjie Ni, Zi Jing Wong, Michael Mrejen, Yuan Wang and Xiang Zhang

*Science* **349** (6254), 1310-1314.  
DOI: 10.1126/science.aac9411

### Wrap-around invisibility cloak

An invisibility cloak can be used to conceal an object from view by guiding light around it. Most cloaks developed so far have bulky structures that are difficult to scale up for hiding large objects. To design a thin invisibility cloak that can be wrapped around an object such as a sheet or skin, Ni *et al.* designed a two-dimensional metamaterial surface. Such flexible, highly reflective materials could be manufactured at large scale to hide large objects.

*Science*, this issue p. 1310

#### ARTICLE TOOLS

<http://science.sciencemag.org/content/349/6254/1310>

#### SUPPLEMENTARY MATERIALS

<http://science.sciencemag.org/content/suppl/2015/09/16/349.6254.1310.DC1>

#### RELATED CONTENT

<http://science.sciencemag.org/content/sci/349/6254/1269.full>

#### REFERENCES

This article cites 46 articles, 10 of which you can access for free  
<http://science.sciencemag.org/content/349/6254/1310#BIBL>

#### PERMISSIONS

<http://www.sciencemag.org/help/reprints-and-permissions>

Use of this article is subject to the [Terms of Service](#)

---

*Science* (print ISSN 0036-8075; online ISSN 1095-9203) is published by the American Association for the Advancement of Science, 1200 New York Avenue NW, Washington, DC 20005. The title *Science* is a registered trademark of AAAS.

Copyright © 2015, American Association for the Advancement of Science